Materials Horizons

Accepted Manuscript

This article can be cited before page numbers have been issued, to do this please use: S. Hwang, H. Yu, H. Ju, H. Kim, J. Y. Baik, Y. Kim, H. S. Kim and H. Lee, *Mater. Horiz.*, 2025, DOI: 10.1039/D5MH01147G.

ROYAL SOCIETY OF CHEMISTRY

rsc.li/materials-horizons

View Article Online
DOI: 10.1039/D5MH01147G

In situ Study of Visible Light-Activated Photocatalytic Conversion Reaction Enhancement of Biomass Using a Magnetic Heterostructure

Sunyoung Hwang,[a, ‡] Hyejin Yu,[b, ‡] Hyeon-Ah Ju,[c,‡], Heewon Kim,[a] Jaeyoon Baik,[d] Young-Min Kim[c*], Hyun Sung Kim[*,b], Hangil Lee[*,a]

[a] Department of Chemistry and Research Institute of Natural Sciences, Sookmyung Women's University, Seoul 04310, Republic of Korea

[b] Department of Chemistry, Pukyong National University, Busan 48513, Republic of Korea

[c] Department of Energy Science, Sungkyunkwan University (SKKU), Suwon 16419, Republic of Korea, Center for 2D Quantum Heterostructures, Institute for Basic Science (IBS), Suwon 16419, Republic of Korea

[d] Beamline Research Division, Pohang Accelerator Laboratory (PAL), Pohang 37673, Republic of Korea

New concepts

The environmental impact of cadmium-based photocatalysts has long posed a paradox in solar-driven catalysis: high photocatalytic efficiency comes at the cost of toxic material use and limited recoverability. In this work, we introduce a magnetically recoverable CdS/Fe_3O_4 heterostructure that not only addresses the sustainability challenge of CdS reuse but also enhances photocatalytic activity via interfacial defect engineering. Unlike conventional heterojunction designs, this system exploits the formation of S–O bonds and oxygen vacancies at the CdS/Fe_3O_4 interface to induce local electronic structure modulation, promoting effective charge separation and reactive oxygen species (ROS) generation. In situ XPS and nanoscale STEM-EELS analyses reveal the dynamic interfacial charge redistribution under visible light, establishing a new paradigm for defect-modulated, multifunctional heterostructures with simultaneous activity and recyclability in biomass-derived molecule oxidation.

View Article Online
DOI: 10.1039/D5MH01147G

Data Availability Statement

The datasets used and/or analysed during the current study available from the corresponding author on reasonable request.

View Article Online
DOI: 10.1039/D5MH01147G

COMMUNICATION

In situ Study of Visible Light-Activated Photocatalytic Conversion Reaction Enhancement of Biomass Using a Magnetic Heterostructure

Received 00th January 20xx,
Accepted 00th January 20xx

DOI: 10.1039/x0xx00000x

Sunyoung Hwang[a‡], Hyejin Yu[b‡], Hyeon-Ah Ju[c‡], Heewon Kim[a], Jaeyoon Baik[d], Young-Min Kim*[c], Hyun Sung Kim*[b], Hangil Lee*[a]

Although cadmium sulfide (CdS) is a promising visible light-active photocatalyst, it is highly toxic. Therefore, in addition to improving the photocatalytic properties of CdS, enhancing its recoverability would allow for more environmentally friendly photocatalytic reactions. In this study, ferrimagnetic Fe_3O_4 nanoparticles (NPs) were added to CdS to form a heterostructure, and photocatalytic CdS NPs were efficiently recovered. The photocatalytic reaction efficiency of this heterostructure for biomass conversion was measured. Using the CdS/Fe_3O_4 heterostructure system, the photocatalytic conversion rates of 5-hydroxymethylfurfural to 5-formylfuran-2-carboxylic acid and toluene to benzaldehyde were approximately 30% and 63% higher, respectively, than those achieved using pristine CdS NPs. Furthermore, the magnetic properties were reduced by only ~6.8% compared to those of Fe_3O_4 NPs, confirming their applicability. The CdS/Fe_3O_4 heterostructure had better photocatalytic properties than CdS, and the magnetic properties were on par with those of Fe_3O_4. Changes in the electronic structure of the heterostructure system were monitored using *in situ* X-ray photoelectron spectroscopy during visible light irradiation and characterized using electron energy-loss spectroscopy in scanning transmission electron microscopy to analyze the defect structure changes occurring at the interface of the heterostructure system.

Introduction

Currently, visible light-activated photocatalysis research focuses on developing highly efficient and low-cost photocatalysts, mainly CdS nanoparticles (NPs) and their derivatives.[1,2] However, CdS photocatalysts suffer from high electron–hole recombination rates, a major weakness of semiconductor NPs, which limits the scope for efficiency enhancement.[3,4] Therefore, several strategies have been developed to compensate for this serious problem. Among them, heterostructures composed of two materials with complementary properties have attracted considerable attention. For enhanced photocatalytic activity, holes and electrons must be readily generated and separated on the NP surface under visible light irradiation. Thus, efficiently generating and separating photogenerated holes and electrons on the surface of the photocatalyst system under visible light is essential to enhance photocatalytic activity. In the design of CdS-based heterostructured photocatalysts, the valence band (VB) and conduction band (CB) edges of CdS and secondary semiconductor NPs are aligned in a staggered configuration. This arrangement facilitates the transfer of photogenerated holes to CdS with a higher VB edge, whereas photogenerated electrons are transferred to secondary semiconductor NPs with a lower CB edge.[5] This allows for selective, facile oxidation reactions of energy-relevant molecules because CdS-based semiconductors can form suitable heterojunctions when combined with materials with lower CB edges. In a type-II heterojunction, the VB and CB edges of CdS and metal oxide (MO) NPs adopt a staggered alignment.[6] This configuration facilitates the migration of photogenerated electrons from CdS to the MO NPs owing to the lower CB edge of the MO NPs relative to that of the CdS NPs. Consequently, the type-II heterojunction promotes effective charge separation between the two components, enhancing their photocatalytic performance. Therefore, fabricating type-II heterojunctions is a viable approach for enhancing photocatalytic activity. In this study, we focused on type-II heterojunctions for oxidizing biomass molecules.

[a] Department of Chemistry and Research Institute of Natural Sciences, Sookmyung Women's University, Seoul 04310, Republic of Korea

[b] Department of Chemistry, Pukyong National University, Busan 48513, Republic of Korea

[c] Department of Energy Science, Sungkyunkwan University (SKKU), Suwon 16419, Republic of Korea, Center for 2D Quantum Heterostructures, Institute for Basic Science (IBS), Suwon 16419, Republic of Korea

[d] Beamline Research Division, Pohang Accelerator Laboratory (PAL), Pohang 37673, Republic of Korea

†Electronic Supplementary Information (ESI) available: [details of any supplementary information available should be included here]. See DOI: 10.1039/x0xx00000x

In addition to increasing the efficiency of visible light-activated CdS-based photocatalytic NPs, another challenge that should be considered is the recovery rate to minimize the detrimental environmental impact of photocatalytic processes. CdS is inherently toxic, and its indiscriminate use is potentially catastrophic to the global environment. Therefore, developing eco-friendly alternatives with similar photocatalytic performance or new, efficient recovery methods is essential.[7] Owing to their magnetic properties and band gap of ~1.8 eV, Fe_3O_4 NPs are good candidates for fabricating visible light-active CdS-based eco-friendly heterostructured photocatalysts.[8] However, Fe_3O_4 NPs exhibit intrinsically poor photocatalytic activity and must form heterostructures to significantly enhance their performance.[9] For this purpose, CdS/Fe_3O_4 heterojunction photocatalysts were synthesized using a simple method to enhance their visible light-active photocatalytic performance and maximize the sample recovery rate. The properties of the CdS/Fe_3O_4 heterostructure system were also analyzed; particularly, the interfacial interactions between heterojunction photocatalysts were investigated. Additionally, their photocatalytic performance was compared with those of pristine CdS and Fe_3O_4 NPs to confirm that the heterojunction composition affected the photocatalytic activity. Furthermore, various characterization studies indicated that the CdS/Fe_3O_4 heterostructures exhibited photocatalytic properties that were superior to those of CdS. The recovery rates were also notable, where the CdS/Fe_3O_4 heterostructures showed a good recovery rate owing to the ferrimagnetic nature of the Fe_3O_4 NPs. Therefore, forming heterostructures consisting of Fe_3O_4 NPs, which have intrinsic magnetic properties but poor photocatalytic performance, and CdS, which has good photocatalytic performance, is expected to yield effective, environmentally friendly photocatalysts.[10]

To achieve the dual goal of increasing photocatalytic activity and recovery, Fe_3O_4 NPs were combined with CdS NPs to create CdS-based type-II heterostructures.[11] Owing to the interfacial contact between CdS and Fe_3O_4 NPs, a simple strategy to increase the photocatalytic efficiency is to enhance the formation of defect structures at this interface. Furthermore, charge transfer in the heterostructures is expected owing to the bonding between the sulfur in CdS and the oxygen in the MO NPs (–S–O–).[6,12] This phenomenon enhances the photocatalytic activity of the heterostructure by modulating the local valence states of neighbouring cations on the atomic scale, allowing the defect structures to act as mobile electron donors.[13]

In this study, we focused on heterojunction systems to increase the efficiency of the oxidation of biomass molecules.[14] To address the versatility of these enhanced photocatalysts, two potential applications were investigated: photocatalytic conversion (PCR) of 5-hydroxymethylfurfural (HMF) and toluene.[15,16] HMF is a biomass-derived platform chemical that is oxidized into 2,5-furandicarboxylic acid (FDCA), providing a green alternative to petroleum-based terephthalic acid.[17] Toluene is a biomass-derived platform chemical that is oxidized into benzaldehyde (BAD), which must be degraded owing to its high volatility, environmental persistence, and toxic effects on ecosystems. The CdS/Fe_3O_4 heterostructure demonstrated multifunctionality as a photocatalyst, achieving superior oxidation of HMF (96% conversion rate) and toluene (82% conversion rate). Therefore, the enhanced photocatalytic activity of the CdS/Fe_3O_4 heterostructure can be attributed to forming a defect structure at its interface.

Previously, several research groups reported the concept for magnetic heterostructures.[18,19] In other words, the concept of heterostructures containing Fe_3O_4 is not entirely new, but we have systematized it using a new analytical method. In this study, we focused on *in situ* X-ray photoelectron spectroscopy (XPS) to investigate the photocatalytic activity of the heterostructure system under visible light irradiation.[20] Specifically, while monitoring the electronic structures of the heterostructure system using XPS, we irradiated the structures with visible light (λ = 445 nm). This allowed us to analyze the changes in the active photocatalytic sites of these systems, providing a mechanistic understanding of the photocatalytic systems. Additionally, scanning probe-based electron energy loss spectroscopy (EELS) was used to investigate the change in electronic structure occurring at the interface of the two NPs (CdS and Fe_3O_4) that comprise the heterostructure and to determine the cause of photocatalytic enhancement.

The results of the PCR of HMF and toluene under visible light irradiation revealed significantly enhanced activities of the CdS/Fe_3O_4 heterostructure, which was thought to result from an increase in the defect structure owing to the formation of S–O bonds at the heterostructure interface. Conversely, CdS/Fe_3O_4 showed no significant degradation in magnetic properties compared with pristine Fe_3O_4 NPs. This result indicates that the formation of the heterostructure does not cause any structural changes in Fe_3O_4 NPs. These compelling results indicate that the various approaches used in this study are promising for developing high-performance photocatalysts capable of addressing numerous environmental challenges.

Results and Discussion

Crystal Structure Characterization

A series of CdS/ Fe_3O_4 heterostructures, denoted as Fe_3O_4(x) (x = 25, 50, and 75 wt%, where x represents the weight percentage of Fe_3O_4), were prepared to optimize photocatalytic performance. The HRTEM images in Figure 1 show the crystal structure of the CdS/Fe_3O_4(50) (Figure 1a and 1b) as the representative heterostructure system. The corresponding atomic-scale fast Fourier transform (FFT) images were simultaneously obtained (Figure 1b, right panels). As shown in the magnified images of the CdS/Fe_3O_4(50) system (Figure 1b, the region marked by the yellow box in Figure 1a), the two samples exhibit distinct single-crystal orientations at the interface (marked by green dashed line), which is also evident in the corresponding FFT images.[21] The CdS (101) interplanar distance in the CdS/Fe_3O_4(50) heterostructure was 3.110 Å, which is similar to that of pure CdS (3.10 Å). Additionally, the Fe_3O_4 (311) interplanar distance in the heterostructures was 2.653 Å, which is comparable to that of pure Fe_3O_4 (2.65 Å); in other words, this distance was not significantly changed by

View Article Online
DOI: 10.1039/D5MH01147G

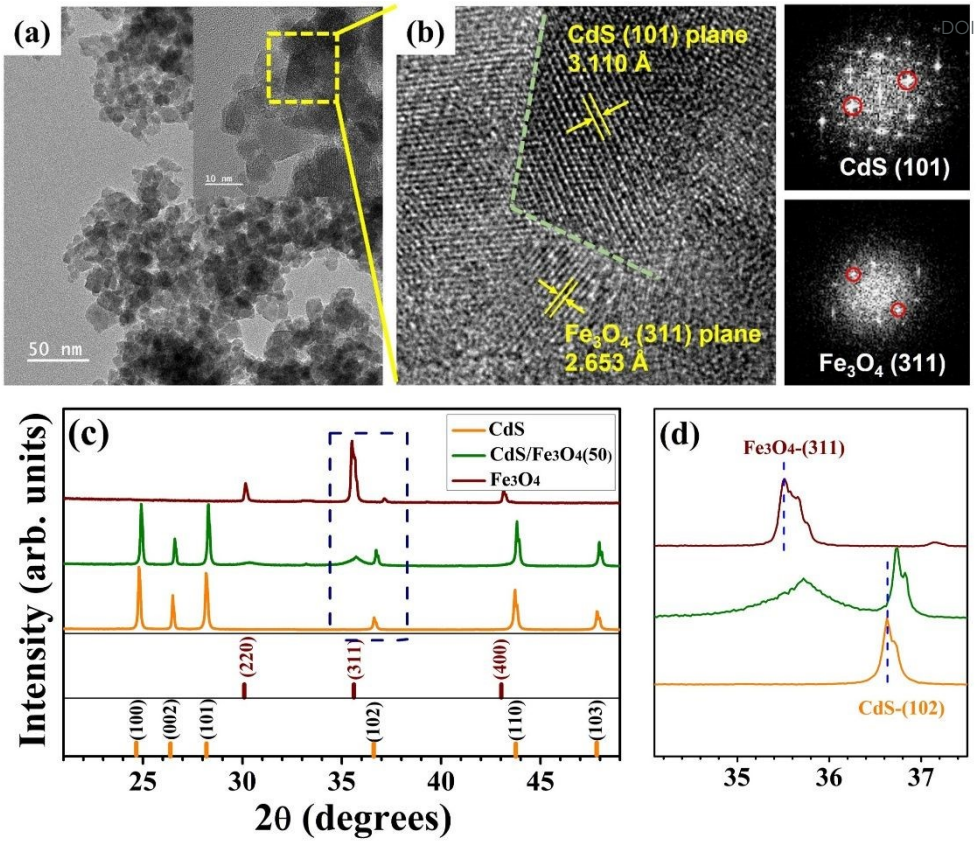

Figure 1. (a), (b) HRTEM images and corresponding FFT images of CdS/Fe_3O_4 heterostructure system; (c), (d) XRD patterns of (c) CdS/Fe_3O_4 and (d) CdS/Fe_3O_4 (50) heterostructure at low scattering angles.

heterostructure formation.[22-24] Therefore, in this study, we focused on the interfacial activity at the contact surface between the two samples to investigate the changes in their photocatalytic properties (see Figure 4). Figure S1 shows the HRTEM images of the Fe_3O_4 and CdS NPs, which were obtained to confirm the structures of the two types of NPs before forming the heterostructure. As shown in Figure S1c,f, the Fe_3O_4 (311) and CdS (100) interplanar distances were 2.56 and 3.60 Å, respectively, which are consistent with those of the previously reported structures.[25,26] The elemental distribution of the synthesized CdS/Fe_3O_4(50) heterostructure was analyzed using energy-dispersive X-ray spectroscopy (EDX), which revealed that Cd, S, Fe, and O were homogeneously distributed throughout the heterostructure (Figure S2).

Powder X-ray diffraction (PXRD) was used to assess the crystallinity and crystal structure of the CdS/Fe_3O_4 series and individual NP samples (Figure 1c and Figure S3). The XRD pattern of the pristine CdS NPs (orange) is consistent with that of the hexagonal wurtzite phase of CdS (JCPDS No. 41-1049).[27] CdS NP diffraction peaks appeared at 2θ angles of 24.8, 26.5, 28.17, 36.63, 43.72, and 47.84°, which were attributed to the (002), (100), (101), (102), (110), and (103) planes of the pristine CdS NPs, respectively.[28] Similar results with high crystallinity were obtained for the Fe_3O_4 NPs, as shown in the uppermost traces in Figure 1c. The 30.16, 35.52, and 43.14° peaks in the XRD profile of the pristine Fe_3O_4 NPs (Figure 1c, dark red trace) are assigned to the (220), (311), and (400) reflections of Fe_3O_4 (PDF 01-1111).[29] The PXRD patterns of the CdS/Fe_3O_4 series clearly exhibit the characteristic diffraction peaks corresponding to both CdS and Fe_3O_4 nanoparticles, indicating that the formation of the composites occurred without significant alteration in the original crystal structures of the individual components.

The PXRD patterns of bare CdS and the CdS/Fe_3O_4 series exhibit comparable FWHM values for the CdS diffraction peaks, indicating that the crystallite size of CdS remains essentially unchanged upon formation of the heterostructure. A closer comparison of crystallite sizes estimated by the Scherrer equation reveals a slight increase from ~57.6 nm for bare CdS to ~64 nm for the CdS/Fe_3O_4 series as the Fe_3O_4content increases. In contrast, for the Fe_3O_4-related diffraction peaks, the crystallite size decreases markedly from ~30.4 nm in bare Fe_3O_4 to ~11 nm in the CdS/Fe_3O_4 series, despite the clear decrease in FWHM values compared to bare Fe_3O_4. These results are summarized in Table S1. This trend suggests that while CdS crystallite size is only marginally affected, the incorporation into the heterostructure induces significant size reduction in Fe_3O_4 domains, likely due to growth suppression or structural modulation during composite formation.

In detail, after assigning the XRD patterns of the heterostructure system, the changes in the low-angle XRD patterns of the synthesized heterostructures were analyzed (Figure 1d).

View Article Online
DOI: 10.1039/D5MH01147G

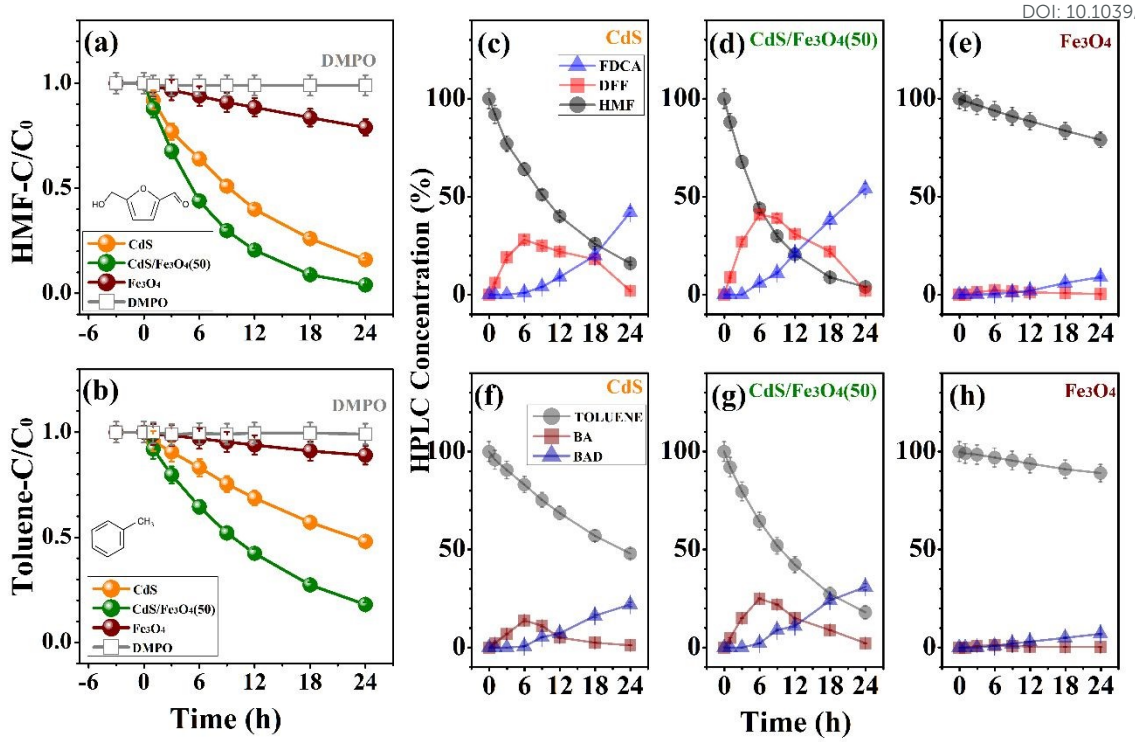

Figure 2. Photocatalytic conversion reactions of (a) HMF and (b) toluene using the CdS/Fe_3O_4(50) heterostructure under 445 nm irradiation over 24 h. Experimental conditions: [catalyst] = 0.015 g/30 mL, $[HMF]_0$ = $[Toluene]_0$ =25 mM, and λ = 445 nm with an illumination intensity of 230 mW/cm². HPLC product analysis for the oxidation of (c–e) HMF and (f–h) toluene using the CdS/Fe_3O_4 heterostructure system.

Differences in the defect structures at the interface of the heterostructure can be inferred from the patterns. The CdS/Fe_3O_4(50) heterostructure produced peaks at larger angles, which is an expected result of forming more defect structures at the interface.[30] These results indicate the successful formation of the CdS/Fe_3O_4 system with heterojunctions. However, the TEM images and XRD patterns alone do not offer direct evidence of defect structures formation, the successful defect construction of the CdS/Fe_3O_4 heterostructure was confirmed through detailed electronic structure analyses and STEM-EELS, as discussed in a later section.

Photocatalytic Performance

To assess the photocatalytic performance of the series of CdS/Fe_3O_4 heterostructure, the PCR was performed by exposing a liquid suspension of two candidate molecules (HMF and toluene) to visible light irradiation (λ = 445 nm) with 230 mW/cm² of illumination intensity. As shown in Figure S4, among the CdS/Fe_3O_4(x) heterostructures, CdS/Fe_3O_4(50) exhibited the highest photocatalytic performance in the photo-conversion reactions (PCR) of both HMF and toluene.

To highlight the superior activity of the CdS/Fe_3O_4 heterostructure, Figure 2 compares the photocatalytic conversion rates and corresponding product yields for HMF and toluene oxidation using CdS/Fe_3O_4(50) with those obtained from the individual CdS and Fe_3O_4 nanoparticles under visible light irradiation.[32,33] Under visible light irradiation, the PCR activity of HMF and toluene was enhanced when the heterostructure system was used instead of pristine CdS and Fe_3O_4 (Figure 2a and b). As a result, the CdS/Fe_3O_4(50) exhibited better PCR efficiencies than the CdS NPs, indicating that the heterostructures are sufficient to promote significant photocatalytic activity. This finding implies that the superior activity of the heterostructures underscores their crucial role in maximizing the concentration of $V_o s$ and optimizing the electronic properties for efficient photocatalysis under visible light irradiation.

Figure 2c–h shows the variation in the yields of FDCA and BAD, the end products of the HMF and toluene oxidation reactions, respectively, as a function of time under visible light irradiation using the CdS/Fe_3O_4(50). The yields of FDCA and BAD followed the same trend as the HMF and toluene PCRs (Figure 2c–h), with the highest yields of FDCA and BAD obtained using the heterostructure system. HMF contains alcohol (–OH) and aldehyde (–CHO) functional groups. Selectively oxidizing –OH or –CHO leads to forming 2,5-diformylfuran (DFF) or 5-hydroxymethyl-2-furancarboxylic acid (HMFCA) as intermediates. Because selectively oxidizing the –OH or –CHO groups of HMF is crucial for the synthesis of FDCA via photocatalysis, identifying the functional groups involved in HMF oxidation by the CdS/Fe_3O_4(50) (Figure 2c–e) is crucial.[34] In these catalytic systems, the –OH group of HMF was selectively oxidized to a –CHO group in all samples, resulting in the formation of 2,5-diformylfuran (DFF) as the sole intermediate, which was subsequently converted to 2,5-furandicarboxylic acid (FDCA) as the final product.[35] In the case of toluene, which

View Article Online
DOI: 10.1039/D5MH01147G

contains a single functional group (–CH_3), oxidation initially produced benzyl alcohol (BA) as the primary intermediate, which was further oxidized to benzaldehyde (BAD) as the final product (Figure 2f–h).

heterostructure system can trap electrons and O_2 to promote the formation of $\bullet O_2^-$. As a result, HMF (or toluene) is converted to FDCA (or BAD) via photocatalytic oxidation under the action of $\bullet O_2^-$ and h^+. To confirm the involvement of reactive oxygen

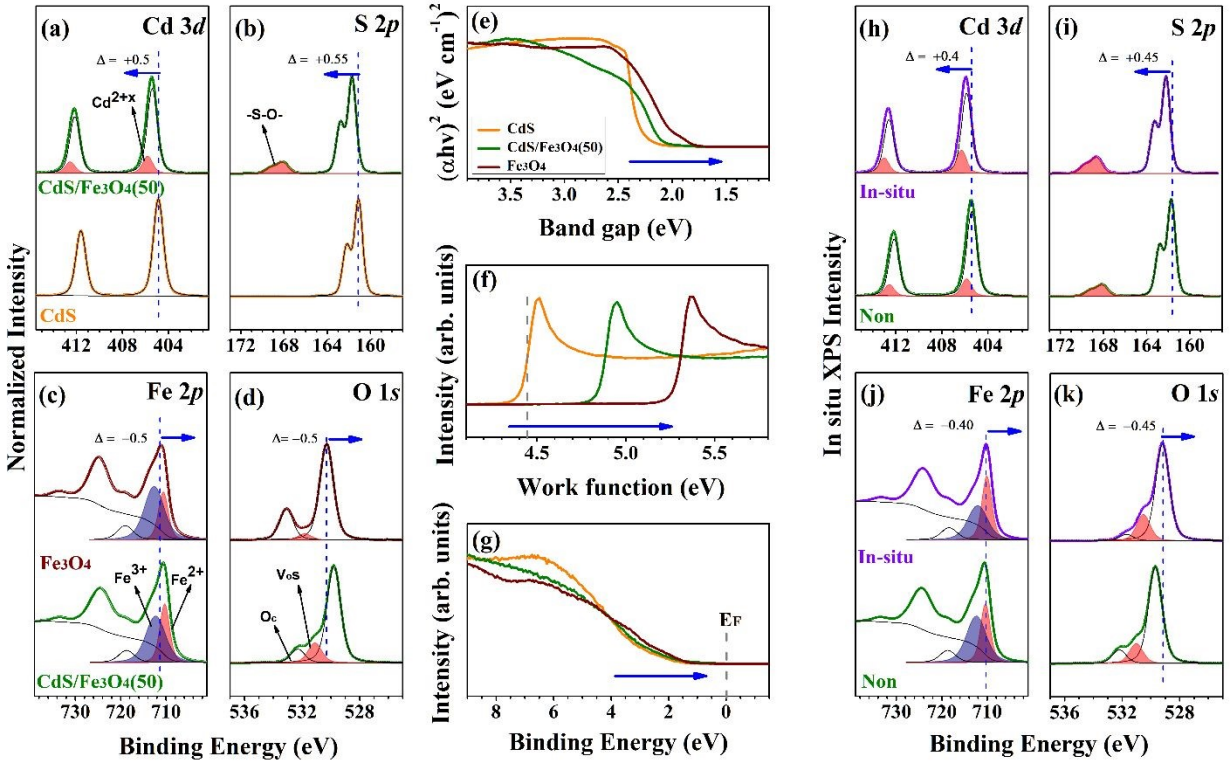

Figure 3. (a) Cd 3*d*, (b) S 2*p*, (c) Fe 2*p*, and (d) O 1*s* XPS spectra for the CdS, Fe_3O_4 and CdS/Fe_3O_4(50). (e) UV–Vis diffuse reflectance spectra and (f) work functions, and (g) valence band spectra of the for the CdS, Fe_3O_4 and CdS/Fe_3O_4(50) (orange – CdS; green – CdS/Fe_3O_4; dark red – Fe_3O_4). (h)–(k) *In situ* XPS spectra of CdS/Fe_3O_4(50) acquired under 445 nm irradiation: (h) Cd 3*d*, (i) S 2*p*, (j) Fe 2*p*, and (k) O 1*s* (green – non-CdS/Fe_3O_4; violet – *in situ* CdS/Fe_3O_4).

Table 1. Relative concentrations (C/C_0) of HMF and toluene and quantities of FDCA and BAD obtained after 24 h of HMF and toluene photocatalytic conversion under 445 nm irradiation using the CdS/Fe_3O_4 heterostructure

	Fe_3O_4	CdS/Fe_3O_4(50)	CdS
HMF (C/C_0)	0.79 ± 0.039	0.04 ± 0.002	0.16 ± 0.008
Yield of FDCA (%)	9.0 ± 0.45	54.1 ± 2.70	42.1 ± 2.10
Toluene (C/C_0)	0.89 ± 0.045	0.18 ± 0.009	0.48 ± 0.024
Yield of BAD (%)	6.9 ± 0.35	31.1 ± 1.55	21.9 ± 1.10

* C and C_0 represent the time-dependent and initial concentrations of HMF and toluene, respectively.

In conclusion, the selective oxidation of biomass-derived molecules (HMF and toluene) using a CdS/Fe_3O_4 heterostructure system dispersed in aqueous solution confirmed that under all conditions, the reaction proceeds from HMF via DFF to the final product FDCA and from toluene via BA to BAD.[36,37] Table 1 lists the 24-hour PCD profiles of HMF, toluene, and the final products (FDCA and BAD) formed using the CdS/Fe_3O_4(50) under 445 nm irradiation.

The proposed mechanism for the photocatalytic oxidation of HMF to FDCA and of toluene to benzaldehyde using the heterostructure system can be described as follows (Scheme S1). The defect structure formed at the interface of the

species such as $\bullet O_2^-$ in the photocatalytic system, we used 5,5-dimethyl-1-pyrroline *N*-oxide (DMPO) as an $\bullet O_2^-$ radical scavenger, which completely inhibited the photocatalytic activity (Figures 2a and 2b).[38] Furthermore, to verify the involvement of active O_2 species such as $\cdot O_2^-$ and $^1O_2$ in the CdS/Fe_3O_4(50) photocatalytic system, electron spin resonance spectroscopy was performed using DMPO and 2,2,6,6-tetramethylpiperidine (TMP) as trapping agents to detect $\cdot O_2^-$ and $^1O_2$ (Figure S5).[39] The signal corresponding to $\cdot O_2^-$ is evident, indicating the contribution of CdS/Fe_3O_4(50) heterostructure to $\cdot O_2^-$ formation (Figure S5a). Similarly, signals corresponding to $^1O_2$ were observed with slight enhancement under visible light irradiation, highlighting the favourable effect of CdS/Fe_3O_4(50) on $^1O_2$ generation. (Figure S5b). Notably, no $\cdot O_2^-$ or $^1O_2$ signals were detected under dark conditions, confirming their origin from the photogenerated carriers of the CdS/Fe_3O_4(50). Consequently, the rapid in situ generation of abundant $\cdot O_2^-$ and $^1O_2$ represents a powerful strategy for the photocatalytic targeted oxidation of HMF to FDCA and toluene to BAD.

A linear correlation between $\ln(C/C_0)$ and the reaction time was obtained for the heterostructure system (CdS/Fe_3O_4(50)), and the PCR processes were fitted to first-order kinetics to determine the first-order rate constants, *k*, for the

photocatalytic reaction of each heterostructure system (Figure S6). As shown in Figure S6a, the *k* values for the PCR of HMF using CdS (orange), CdS/Fe_3O_4(50) (green), and Fe_3O_4 (dark red) were calculated to be 0.076, 0.134, and 0.0098 h^{-1}, respectively. The CdS/Fe_3O_4(50) accelerated the PCR rate of HMF by 76.4% compared with that of the same reaction using CdS. As shown in Figure S6b, the *k* values for the PCR of toluene using CdS (orange), CdS/Fe_3O_4(50) (green), and Fe_3O_4 (dark red) were calculated to be 0.031, 0.071, and 0.0049 h^{-1}, respectively. The CdS/Fe_3O_4(50) accelerated the PCR rate of toluene by 129% compared with that of the same reaction using CdS. Additionally, the photocatalytic activities of the three tested materials were maintained (>97%), even after 10 reuse cycles (Figure S7).

To thoroughly address environmental concerns regarding Cd leaching and confirm the stability of the CdS/Fe_3O_4 heterostructure photocatalyst, additional stability analyses were performed. Elemental composition analysis by X-ray fluorescence (XRF) revealed no significant change in the Cd/Fe elemental ratio before and after the photocatalytic reaction, confirming negligible Cd loss during the reaction and subsequent magnetic recovery (see Table S2). Furthermore, inductively coupled plasma mass spectrometry (ICP-MS) provided quantitative insight into dissolved Cd, showing that the bare CdS photocatalyst exhibited approximately 3% Cd leaching relative to its total Cd content. In sharp contrast, the CdS/Fe_3O_4(50) displayed significantly reduced Cd leaching of less than 1% under identical reaction conditions. These findings clearly illustrate that integrating Fe_3O_4 nanoparticles enhances the structural integrity and environmental safety of CdS-based photocatalysts, highlighting the advantage of this heterostructure approach in terms of catalyst recovery and minimizing environmental risks.

The magnetic properties of the heterostructure systems were evaluated using VSM to determine whether they could be recovered using magnets, which was one of the objectives of this study (Figure S8a).[40] Fe_3O_4 NPs are known to have ferrimagnetic properties at room temperature. The magnetic properties of the Fe_3O_4 NPs and heterostructures prepared under the same conditions were measured.[41] The magnetization of the CdS/Fe_3O_4(50) system decreased by only ~6.8%, from 79.32 emu/g for the pristine Fe_3O_4 system to 73.62 emu/g for the CdS/Fe_3O_4(50), even though it only contained 50% CdS. This indicated that the recovery rate was not significantly affected, confirming the applicability of this system. EPR analyses were also performed to determine the differences in the number of V_os between the heterostructure system and Fe_3O_4 NPs (Figure S8b).[42] As shown in the figure, the EPR spectra of CdS/Fe_3O_4(50) show a pronounced increase in signal intensity at g-factors of ~1.99 each, indicating a Zeeman effect induced by a single electron trapped in V_os.[43] These results confirm that the number of V_os increased in the CdS/Fe_3O_4(50), which is consistent with our observation of the enhanced photocatalytic properties of the CdS/Fe_3O_4(50).[44] Therefore, the CdS/Fe_3O_4(50) gave rise to a higher V_os peak intensity than the Fe_3O_4 NPs, which can be explained by an increase in the number of V_os owing to forming a heterojunction with CdS at the interface. As mentioned, structural analysis and PCR experiments are still insufficient to clearly explain that the CdS/Fe_3O_4(50) we synthesized has a clear heterostructure. To clarify it, we investigated structural changes at the interface using electron structure analysis using XPS and STEM-EELS techniques.

Electronic Structure Characterization

Figure 3a–d illustrate the electronic structure changes captured in the four core-level XPS profiles of the non-irradiated CdS/Fe_3O_4 heterostructure. XPS analyses confirmed that charge carriers were transferred from CdS to Fe_3O_4 in the CdS/Fe_3O_4(50).[45] Therefore, the binding energy shift in this system follows a specific trend: the binding energies of CdS increase, whereas those of Fe_3O_4 decrease. As shown in Figure 3a,b, the binding energies of the two core levels in the pristine CdS NPs (404.8 eV for Cd $3d_{5/2}$ and 161.1 for S $2p_{3/2}$) shifted to significantly higher positions in the spectra of the CdS/Fe_3O_4(50) (405.3 eV for Cd $3d_{5/2}$ and 161.65 for S $2p_{3/2}$).[46] Conversely, Figure 3c,d shows that the binding energies in the two core-level XPS spectra of the pristine Fe_3O_4 NPs (711.1 eV for Fe $2p_{3/2}$ and 530.2 for O 1*s*) shifted to lower binding energies in CdS/Fe_3O_4(50) (710.6 eV for Fe $2p_{3/2}$ and 529.7 for O 1*s*).[47] Thus, we confirmed that charge transfer from CdS to Fe_3O_4 occurred in this heterostructure. Interestingly, we noted a Cd_{2+x} peak (defect-induced structure) in the Cd 3*d* spectrum of the CdS/Fe_3O_4 heterostructure along with a peak corresponding to –S–O– in the S 2*p* spectrum, which is evidence of heterostructure electron transfer owing to changes in CdS (S $2p_{3/2}$ = 167.9 eV). These peaks are attributed to forming a new electronic structure at the interface between the two NPs.[48] Further evidence of interfacial changes was observed for Fe_3O_4. As shown in Figure 3c, the intensity ratio of Fe^{2+} to Fe^{3+} in the Fe $2p_{3/2}$ peak of CdS/Fe_3O_4(50) was remarkable. For pristine Fe_3O_4, the relative intensity of the Fe^{2+}-induced peak is lower than that of the Fe^{3+}-induced peak. However, the structure of Fe_3O_4 in the CdS/Fe_3O_4(50) did not change, but the relative intensity of the Fe^{2+} peak increased owing to an increase in the surface defect structure formed by changes in the electronic structure at the interface. As shown in Figure 3d, the decomposed O 1*s* XPS spectra of both samples include three components: Fe–O (529.7 eV), an oxygen vacancy peak (V_os) (531.7 eV), and a chemisorbed adsorption peak $–O_c$ (532.5 eV). The CdS/Fe_3O_4(50) gave rise to a higher V_os peak intensity than the Fe_3O_4 NPs, which can be explained by an increase in the number of V_os owing to the formation of a heterojunction with CdS at the interface.[49] Table 2 lists the changes in the binding energies obtained via XPS analysis of the heterostructure system.

Table 2. Cd $3d_{5/2}$, S $2p_{3/2}$, Fe $2p_{3/2}$, and O 1*s* binding energies in CdS , CdS/Fe_3O_4(50) and Fe_3O_4.

Core level	CdS	CdS/Fe_3O_4(50)	Fe_3O_4
Cd $3d_{5/2}$	404.8 eV	405.3 eV	-
S $2p_{3/2}$	161.1 eV	161.65 eV	-
Fe $2p_{3/2}$	-	710.6 eV	711.1 eV
O 1s	-	529.7 eV	530.2 eV

View Article Online
DOI: 10.1039/D5MH01147G

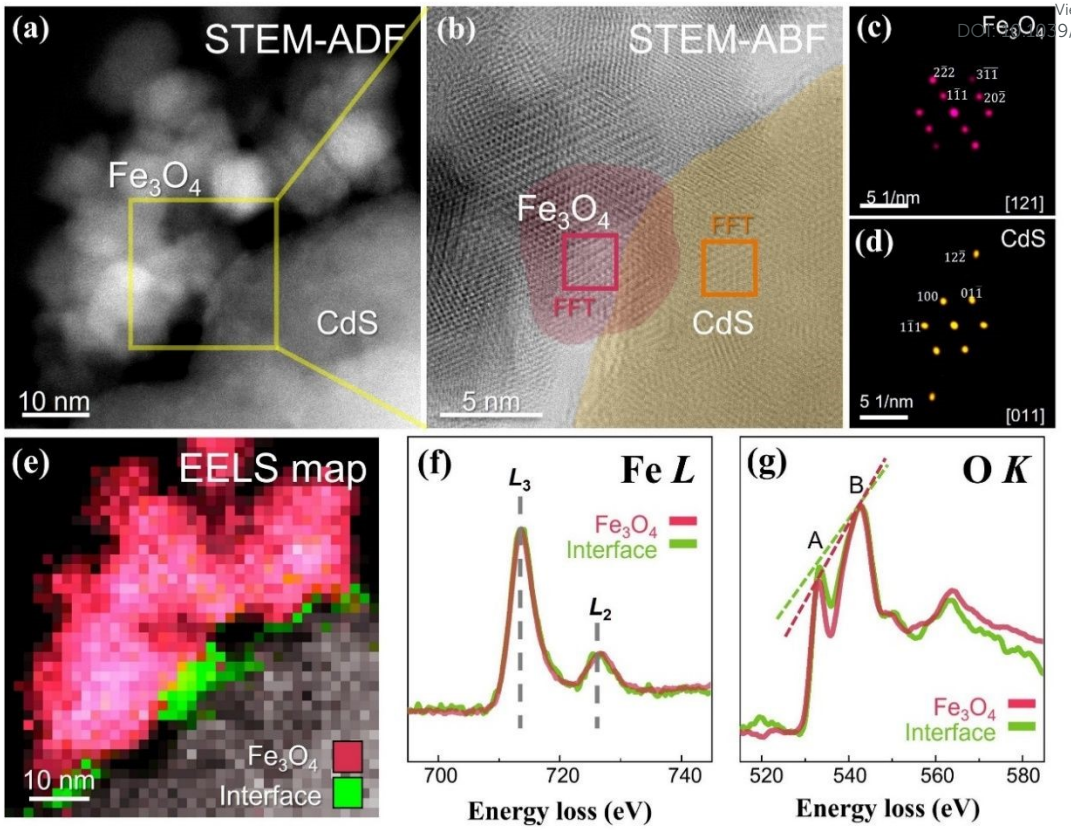

Figure 4. Structural and chemical characterization of the CdS/Fe_3O_4 (50). (a) Annular dark-field (ADF) STEM image and (b) annular bright-field (ABF) STEM image of the CdS/Fe_3O_4 heterostructure, with magnification of the region marked by the yellow box in (a). (c), (d) FFT patterns extracted from the Fe_3O_4 (magenta) and CdS (orange) regions in (b). (e) EELS map distinguishing Fe_3O_4 (magenta), the interface region (green), and CdS (grey) based on chemical distribution differences. Energy loss near-edge structure (ELNES) of (f) Fe *L*-edge and (g) O *K*-edge spectra.

Pristine CdS NPs exhibit strong light absorption in the visible wavelength range owing to their narrow bandgaps.[50] The bandgap of the synthesized CdS NPs, as shown in Figure 3e, was determined to be 2.30 eV from Tauc plots obtained from the DRS results. The bandgap of the Fe_3O_4 NPs, as shown in Figure 3e, was measured to be 1.8 eV.[51] The optical properties and bandgap energies of the heterostructured photocatalysts were confirmed by UV–Vis DRS. The bandgap of the CdS/Fe_3O_4(50) was found to be 2.1 eV, which lies between those of the constituent NPs of the heterostructure, and the bandgap remained within the visible wavelength range, indicating that the CdS/Fe_3O_4(50) exhibited visible light photocatalytic activity. The work function measurements of the heterostructure (Figure 3f) confirm that charge was transferred between CdS and Fe_3O_4.[52] In the CdS/Fe_3O_4(50), the work functions of CdS and Fe_3O_4 were measured to be 4.45 and 5.30 eV, respectively, indicating that the relatively small work function of CdS compared with that of Fe_3O_4 allows charge carriers to move smoothly from CdS to Fe_3O_4.[53, 54] Figure 3g shows valence band spectra to measure the fermi level (EF) of three samples. Each EF of the three samples (CdS, CdS/Fe_3O_4(50), and Fe_3O_4) is measured to 1.75, 1.52, and 1.40 eV, which lies between those of the constituent NPs of the heterostructure.

The photocatalytic properties of the heterogeneous system were predicted to improve owing to the increased number of defect structures formed at the interface. In other words, the electrons and O_2 trapped in these defect structures were converted into $\bullet O_2^-$ and h^+ under visible light irradiation. To gain a deeper understanding of this phenomenon, observing the light-induced changes in the electronic structures of the heterostructure system is necessary. Accordingly, in this study, *in situ* XPS was used to determine the changes occurring during photocatalysis. Figure 3h–k shows the *in situ* XPS results for the CdS/Fe_3O_4(50). As expected, the electronic structure changed upon visible light irradiation: under 445 nm irradiation, the CdS peaks shifted towards higher binding energies, and the Fe_3O_4 peaks shifted towards lower binding energies. These observations confirm the light-induced photocatalytic properties of the heterostructures. In particular, a more significant change is observed for the CdS/Fe_3O_4(50), which is consistent with its superior photocatalytic properties. We also observed an increase in the intensity of the –S–O– component of the S 2*p* peak, indicating charge transfer at the interface, as well as an increase in the intensity of the V_os component of the O 1*s* peak. Thus, the *in situ* XPS results clearly explain the photocatalytic activity of the heterostructure and reveal the underlying reason for the superior visible-light photocatalytic activity of this system compared with that of CdS. The increase in defect structures at the interface between the two materials

in the heterostructure significantly enhanced the photocatalytic properties.

Surface Structure Characterization

To confirm the change in the electronic states at the interface of the CdS/Fe_3O_4(50), we performed nanoscale STEM-EELS SI analysis, as shown in Figure 4.[55,56] We selected an interfacial region between the CdS and Fe_3O_4 NPs for spectral analysis of the heterostructure (highlighted by the yellow box in Figure 4a). Figure S9 shows the EDX mapping results of the four elements comprising the heterostructure interface. The elemental distribution of the synthesized CdS/Fe_3O_4(50) revealed that Cd, S, Fe, and O were distributed in the interfacial region of the heterostructure. The ABF STEM image of the magnified area in the yellow box in Figure 4a shows that the heterostructures of Fe_3O_4 and CdS are in close contact (Figure 4b). Therefore, changes in the electronic structure can be observed at the interface between the two NPs, as confirmed in this study. FFT was used to verify the lattice structures of the two NP types in the heterostructure (i.e., Fe_3O_4 and CdS), as shown in Figure 4c,d. No significant structural changes are apparent, confirming the crystallographic structure of each phase. Therefore, we can assume that the improvement in the photocatalytic properties of the CdS/Fe_3O_4 heterojunction is due to the enhancement of the interfacial defect structures and the change in the interfacial electronic structure. Additionally, Figure S10 shows the Fe *L*-edge and O *K*-edge spectra in the three regions, distinguishing between the interface of the heterogeneous structure, the CdS region, and the Fe_3O_4 region. The two spectra clearly show a reduction in the peak at the interface of the CdS/Fe_3O_4 heterostructure and its disappearance in the CdS region, allowing us to observe changes in the electronic structure at the interface.[57]

The multiple linear least squares (MLLS) fitting method, using the selected EELS components as references, was used to map the local distributions of different electronic and charge states within the EELS SI dataset.[58,59] This approach, which assumes that the total spectrum can be represented as a linear combination of the local component spectra, is traditionally used to distinguish electronically distinct phases at heterostructure interfaces. Figure 4e shows the chemical phase mapping results for the EELS SI data in the Fe_3O_4 region at the heterostructure interface shown in Figure 4b. A heterostructure (green) is formed at the interface between Fe_3O_4 (magenta) and CdS (grey), which is expected to have a different electronic structure. Additionally, the Fe *L*-edge (Figure 4f) and O *K*-edge (Figure 4g) profiles were obtained from the EELS maps. The Fe *L*-edge spectra of Fe_3O_4 and CdS/Fe_3O_4 were almost identical (Figure 4f). This indicates that the change in the photocatalytic properties was not due to a change in the Fe_3O_4 structure itself, which is consistent with the subtle change in the two charge states (Fe^{2+} and Fe^{3+}) in the Fe 2*p* spectrum (Figure 3c). By contrast, in the case of the O *K*-edge spectrum shown in Figure 4g, although the overall shape change is similar, the intensities of the A and B peaks differ, which can explain the change in the defect structure. In other words, the increase in peak A can be explained by the increase in defect structures, and the A/B value (0.74) of the heterostructure increased more than the A/B value (0.68) of Fe_3O_4.[60,61] This result explains the increase in the number of defect structures at the interface. This result agrees well with the change in the oxygen defect structures in the O 1*s* spectrum shown in Figure 3d. As a result, the two spectra obtained from the STEM-EELS mapping can explain the changes at the interface. It is worth noting that a small shift of the A peak towards a higher energy loss was observed by ~0.25 eV. This peak shift may be linked to the probable presence of hydroxylated metal at the interface.[62] However, careful caution should be taken for interpreting the observed small peak shift because dehydroxylation progresses fast under electron beam irradiation under high-vacuum conditions of STEM.

Finally, we examined whether simple physically mixed samples of the two NPs could form heterostructures, in contrast to

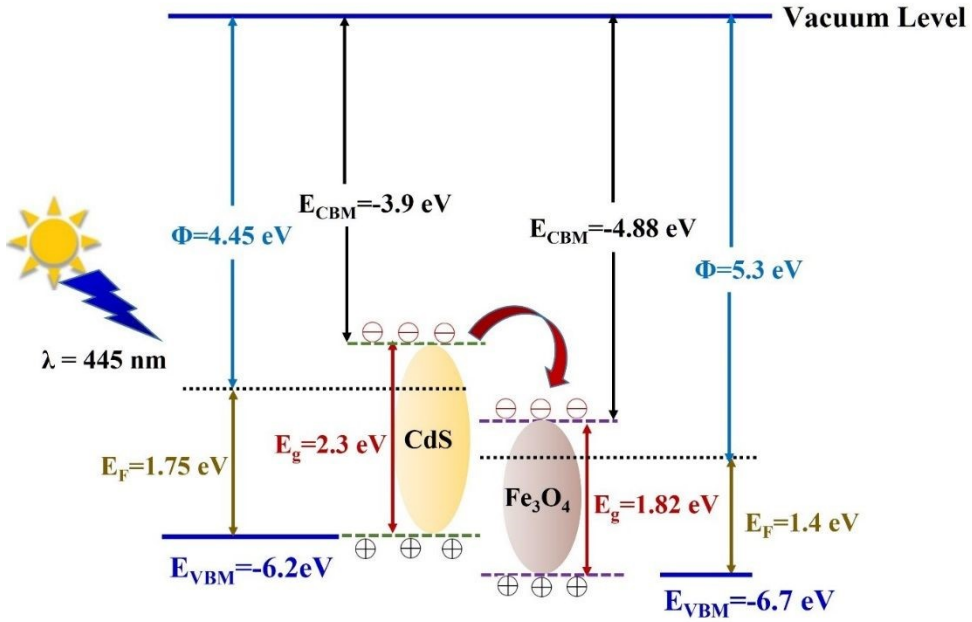

Scheme 1. Illustrations of type-II mechanism for CdS/Fe3O4 heterostructure system.

the methodology described in this work, in which the CdS/Fe_3O_4 heterostructure was synthesized via base treatment. The physically mixed sample, having the same composition as CdS/Fe_3O_4(50), was prepared by grinding CdS and Fe_3O_4 NPs for 10 min in an agate mortar. This comparison allowed us to determine whether the observed hetero-contact originated from the intrinsic nature of the sample or from the base-treatment process, thereby providing direct evidence for our synthesis methodology. As expected, the XPS and PCR experimental results for the physically mixed CdS– Fe_3O_4 sample, shown in Figures S11 and S12, revealed that the photocatalytic properties varied depending on the amount of CdS. Furthermore, the XPS analysis confirmed that no chemical bonds formed between the two components, indicating only mechanical mixing; the CdS and Fe_3O_4NPs remained independent and exhibited nearly identical electronic structures to their pristine counterparts.

Herein, we propose a type-II mechanism for the photooxidation of HMF and toluene using the CdS/Fe_3O_4 heterojunctions, as shown in Scheme 1. The movement of electrons in heterojunction photocatalysts can also be described in terms of the work function of the individual semiconductors. Free electrons migrate from a semiconductor with a smaller work function to one with a larger work function, thereby storing electron density in the latter. Because the work function of Fe_3O_4 is larger than that of CdS (5.3 eV vs 4.45 eV, respectively), free electrons move from the positively charged CdS to the negatively charged Fe_3O_4. This makes CdS highly electropositive and Fe_3O_4 highly electronegative. Consequently, photogenerated electrons and holes can exist under conditions that allow visible light activity. When visible light irradiates the surface of the heterostructure, electrons are excited to the conduction band (CB), and holes remain in the valence band (VB) of the heterostructure. In other words, the recombination of electron–hole pairs is strongly suppressed owing to the efficient separation of the charge carriers.[63] Therefore, the photogenerated electrons and holes were efficiently separated under visible light irradiation. Photogenerated electrons accumulate in the CB of Fe_3O_4, and photogenerated holes accumulate in the VB of CdS under visible light irradiation. To confirm the reaction mechanism, the migration directions of the photogenerated electrons and holes were investigated. The photogenerated electrons were found to initially migrate from the highly negative CB of CdS to the low-energy CB of Fe_3O_4, whereas the holes migrated from the VB of Fe_3O_4 to the VB of CdS. This results in excess electrons in the Fe_3O_4 CB and excess holes in the CdS VB, that is, effective separation of the charge carriers.

Conclusions

In this study, CdS and Fe_3O_4 NPs were synthesized independently, and CdS/Fe_3O_4 heterostructures were prepared as photocatalysts under basic conditions. The results showed that after visible-light irradiation, the heterostructure system exhibited a significant increase in the HMF and toluene oxidation reaction yields by CdS. The CdS/Fe_3O_4 heterostructure, which follows a type-II mechanism, exhibited better PCR efficiency owing to its improved defect structure. A breakthrough was also achieved in terms of the recovery rate of these samples; the magnetic properties of the CdS/Fe_3O_4 heterostructure, containing ferrimagnetic Fe_3O_4, did not significantly degrade compared to those of Fe_3O_4 and exhibited a 100% recovery rate when using a magnet. Thus, the environmental problems that may arise from using photocatalytic NPs can be addressed. A CdS/Fe_3O_4 heterojunction structure with significantly improved photocatalytic properties was developed owing to an increase in the defect structure at the interface between the two materials. Moreover, owing to its magnetic properties, this heterosystem provides a solution for recovering NP catalysts. Its photocatalytic properties are comparable to those of other CdS-based heterojunctions reported in the literature, making the heterostructure highly promising for future applications.

Author Contributions

Sunyoung Hwang: conceptualization, investigation and formal analysis; H. Yu: investigation and formal analysis, Hyeon-Ah Ju: investigation and formal analysis; Heewon Kim: formal analysis, Jaeyoon Baik: formal analysis for high-resolution XPS with the synchrotron radiation, Young-Min Kim: formal analysis and writing – original draft; H.S. Kim: supervision, funding acquisition, writing – review & editing. Hangil Lee: conceptualization, supervision, funding acquisition, writing – review & editing All authors contributed to discussion and manuscript preparation. ‡ Contributed equally.

Data availability

The data supporting this article have been included as part of the ESI.†

Conflicts of interest

The authors declare no competing financial interest.

Acknowledgements

This work was supported by the National Research Foundation of Korea (NRF) funded by the Korean government (MSIP) (NRF-2023R1A2C1007484) and core research institute (CRI) program, basic science research program through the NRF under program number (2022R1A6A1A03051158). Y.-M. Kim acknowledges the support of the National Research Foundation of Korea (NRF) for a grant funded by the Korean government (MSIT) (RS-2023-NR076943). H. Lee acknowledges the National Research Foundation of Korea (NRF) grant, funded by the Korean government (MSIT) (RS-2024-00346153).

Notes and references

1 X. Liu, M. Sayed, C. Bie, B. Cheng, B. Hu, J. Yu and L. Zhang, *J. Materiomics*, 2021, **7**, 419.

2 K. Yang, Z. Yang, C. Zhang, Y. Gu, J. Wei, Z. Li, C. Ma, X. Yang, K. Song, Y. Li, Q. Fang and J. Zhou, *Chem. Eng. J.*, 2021, **418**, 129344.
3 J. Zhang, G. Yang, B. He, B. Cheng, Y. Li, G. Liang and L. Wang, *Chin. J. Catal.*, 2022, **43**, 2530.
4 N. Venkatesh, K. Sabarish, G. Murugadoss, R. Thangamuthu and P. Sakthivel, *Environ. Sci. Pollut. Res.*, 2020, **27**, 43212.
5 L. Wang, H. Wei, Y. Fan, X. Gu and J. Zhan, *J. Phys. Chem. C*, 2009, **113**, 14119.
6 H. Yu, D. T. Hoang, H. S. Kim and H. Lee, *J. Mater. Chem. A*, 2025, **13**, 6049.
7 H.-A. Ju, D. T. Hoang, W.-S. Jang, Y.-H. Kim, E.-B. Park, S.-H. Yang, K. Ihm, Y.-M. Kim and H. Lee, *Appl. Surf. Sci.*, 2025, **679**, 161197.
8 S. Pal, A. Kumar, S. Kumar, A. K. De, R. Prakash and I. Sinha, *Catal. Lett.*, 2022, **152**, 3259.
9 L. Shi, X. Wang, Y. Hu and Y. He, *Sol. Energy*, 2020, **196**, 505.
10 X. Liu, Z. Fang, X. Zhang, W. Zhang, X. Wei and B. Geng, *Cryst. Growth Des.*, 2009, **9**, 197.
11 A. Samadi-Maybodi, M. R. Shariati and A. H. Colagar, *ChemPlusChem*, 2018, **83**, 769.
12 R. K. Chava, N. Son and M. Kang, *Appl. Surf. Sci.*, 2021, **556**, 149731.
13 Z. Khan, T. R. Chetia, A. K. Vardhaman, D. Barpuzary, C. V. Sastri and M. Qureshi, *RSC Adv.*, 2012, **2**, 12122.
14 C. Shi, Y. An, G. Gao, J. Xue, H. Algadi, Z. Huang and Z. Guo, *ACS Sustain. Chem. Eng.*, 2024, **12**, 2538.
15 C. Li, J. Li, L. Qin, P. Yang and D. G. Vlachos, *ACS Catal.*, 2021, **11**, 11336.
16 L. Sun, G. Li, S. Wan and T. An, *Chemosphere*, 2010, **78**, 313.
17 D. J. Aranha and P. R. Gogate, *Ind. Eng. Chem. Res.*, 2023, **62**, 3053.
18 L. Wang, H. Wei, Y. Fan, X. Gu, *J. Zhan, J. Phys. Chem. C* 2009, **113**, 14119.
19 Z. Wu, H. Yu, L. Kuai, H. Wang, T. Pei, B. Geng, *J. Colloid Interface Sci.* 2014, **426**, 83.
20 V. N. Pham, S. Lee, H. Lee and H. S. Kim, *Inorg. Chem.*, 2023, **62**, 3703.
21 L. Wang, H. Wei, Y. Fan, X. Gu and J. Zhan, *J. Phys. Chem. C*, 2009, **113**, 14119.
22 Y. Zhu, J. Chen, L. Shao, X. Xia, Y. Liu and L. Wang, *Appl. Catal., B*, 2020, **268**, 118744.
23 Y. Cheng, Y. Wang, F. Bao and D. Chen, *J. Phys. Chem. B*, 2006, **110**, 9448.
24 X. Bian, K. Hong, L. Liu and M. Xu, *Appl. Surf. Sci.*, 2013, **280**, 349.
25 A. Khalid, R. M. Ahmed, M. Taha and T. S. Soliman, *J. Alloys Compd.*, 2023, **947**, 169639.
26 X. Jin, Y. Fang, T. Salim, M. Feng, Z. Yuan, S. Hadke and L. H. Wong, *Adv. Mater.*, 2021, **33**, 2104346.
27 A. Phuruangrat, T. Thongtem and S. Thongtem, *Mater. Lett.*, 2012, **80**, 114.
28 K. Zhang, Z. Mou, S. Cao, S. Wu, X. Xu and C. Li, *Int. J. Hydrogen Energy*, 2022, **47**, 12605.
29 M. A. Sabur and M. A. Gafur, *J. Nanomater.*, 2024, 9577778.
30 S. Muruganandam, G. Anbalagan and G. Murugadoss, *Appl. Nanosci.*, 2015, **5**, 245.
31 L. Saravanan, A. Pandurangan and R. Jayavel, *J. Nanopart. Res.*, 2011, **13**, 1621.
32 V. N. Pham, H. Jeon, S. Hong and H. Lee, *Inorg. Chem.*, 2022, **61**, 16887.
33 J. Cui, K. K. Niu, R. Z. Zhang, H. Liu, S. Yu and L. B. Xing, *Chem. Commun.*, 2024, **60**, 4310.
34 W. Zhang, H. Qian, Q. Hou and M. Ju, *Green Chem.*, 2023, **25**, 893.
35 W. Wu, G. Zhang, J. Zhang, G. Wang, C. H. Tung and Y. Wang, *Chem. Eng. J.*, 2021, **404**, 126433.
36 Z. Zhang and K. Deng, *ACS Catal.*, 2015, **5**, 6529.
37 R. Li, H. Kobayashi, J. Guo and J. Fan, *J. Phys. Chem. C*, 2011, **115**, 23408.
38 H. Jeon, D. T. Hoang, J. Baik, S. Hong and H. Lee, *Inorg. Chem.*, 2024, **63**, 12370.
39 D. Sasikumar, Y. Takano, H. Zhao, R. Kohara, M. Hamada, Y. Kobori and V. Biju, *Sci. Rep.*, 2022, **12**, 11371.
40 G. Xu, M. Du, T. Li, Y. Guan and C. Guo, *Sep. Purif. Technol.*, 2021, **275**, 119157.
41 F. Soltani-Nezhad, A. Saljooqi, A. Mostafavi and T. Shamspur, *Ecotoxicol. Environ. Saf.*, 2020, **189**, 109886.
42 H. Zhang, S. Gan, D. Hou, X. Q. Qiao, R. Chi and D. S. Li, *Catal. Sci. Technol.*, 2023, **13**, 1196.
43 J. He, Y. Mei and W. C. Zheng, *Optik*, 2019, **194**, 163087.
44 S. Omar, M. Omar, N. F. Attia, G. M. El-Subruiti and A. Eltaweil, *Surf. Interfaces*, 2024, **45**, 103817.
45 Z. Zheng, F. Han, B. Xing, X. Han and B. Li, *J. Colloid Interface Sci.*, 2022, **624**, 460.
46 Y. Liu, L. Zhou, Y. Hu, C. Guo, H. Qian, F. Zhang and X. W. D. Lou, *J. Mater. Chem.*, 2011, **21**, 18359.
47 T. Li, M. Wang and Y. Hao, *Sci. Total Environ.*, 2023, **857**, 159254.
48 Y. Wang, L. Zhao, X. Cai, Y. Chen, J. Xu, L. Zhang, X. Lin, X. Dai, Y. Jiang, J. Liao and Y. Zhang, *Environ. Sci. Pollut. Res.*, 2024, **31**, 15091.
49 A. Aguinaco, J. M. Mánuel, E. Blanco, M. Domínguez, R. Litrán, J. J. Delgado and M. Ramírez-del-Solar, *Materials*, 2022, **15**, 6718.
50 Q. Li, B. Guo, J. Yu, J. Ran, B. Zhang, H. Yan and J. R. Gong, *J. Am. Chem. Soc.*, 2011, **133**, 10878.
51 A. Raza, H. Shen, A. A. Haidry and S. Cui, *Appl. Surf. Sci.*, 2019, **488**, 887.
52 X. Wei, T. Xie, L. Peng, W. Fu, J. Chen, Q. Gao, G. Hong and D. Wang, *J. Phys. Chem. C*, 2011, **115**, 8637.
53 Z. He, Y. Fang, X. Wang and H. Pang, *Synth. Met.*, 2011, **161**, 420.
54 L. Wang, B. Cheng, L. Zhang and J. Yu, *Small*, 2021, **17**, 2103447.
55 R. Luo, M. Gao, C. Wang, J. Zhu, R. Guzman and W. Zhou, *Adv. Funct. Mater.*, 2024, **34**, 2307625.
56 M. de la Mata and S. I. Molina, *Nanomaterials*, 2022, **12**, 337.
57 S. Sun, X. Li, C. Zhang, X. Wang, J. Wang, C. Wang and Y. Bai, *Adv. Mater.*, 2024, **36**, 2405876.
58 B. Sun, Z. Liang, Y. Qian, X. Xu, Y. Han and J. Tian, *ACS Appl. Mater. Interfaces*, 2020, **12**, 7257.

View Article Online
DOI: 10.1039/D5MH01147G

View Article Online
DOI: 10.1039/D5MH01147G

59 W. S. Jang, Y. Jin, Y. H. Kim, S. H. Yang, S. J. Kim, J. A. Hong, J. Lee, H. Lee and Y. M. Kim, *Appl. Catal., B: Environ.*, 2022, **305**, 121083.
60 M. H. Aguirre, A. Shkabko and A. Weidenkaff, *Cryst. Growth Des.*, 2010, **10**, 3562.
61 H. S. Kim, Y. J. Kim, Y. R. Son, V. N. Pham, K. J. Kim, C. W. Kim and H. Lee, *Sci. Rep.*, 2022, **12**, 11295.
62 N. Senamart, K. Deekamwong, J. Wittayakun, S. Prayoonpokarach, N. Chanlek, Y. Poo-arporn, S. Wannapaiboon, P. Kidkhunthod and S. Loiha, *Rsc Adv*, 2022, **12**, 25578-25586.
63 A. Samadi-Maybodi, M. R. Shariati and A. H. Colagar, *ChemPlusChem*, 2018, **83**, 769.